A stochastic model of geomorphic risk due to episodic river aggradation and degradation

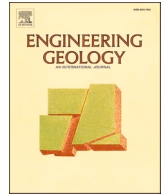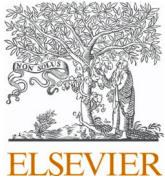Chen, Tzu Yin Kasha; Hung, Chi Yao; Chiang, Yu Chou; Hsieh, Meng Long; Capart, Hervé

Important note
To cite this publication, please use the final published version (if applicable).
Please check the document version above.

A stochastic model of geomorphic risk due to episodic river aggradation and degradation

Tzu-Yin Kasha Chen [a], Chi-Yao Hung [b,*], Yu-Chou Chiang [c], Meng-Long Hsieh [d], Hervé Capart [a]

[a] *Dept of Civil Engineering and Hydrotech Research Institute, National Taiwan University, No. 1, Section 4, Roosevelt Rd., 10617 Taipei, Taiwan*
[b] *Dept of Soil and Water Conservation, National Chung Hsing University, No. 145, Xingda Rd., 402 Taichung, Taiwan*
[c] *Faculty of Architecture and the Built Environment, Delft University of Technology, Julianalaan 134, 2628 BL Delft, The Netherlands*
[d] *Dept of Earth and Environmental Sciences, National Chung Cheng University, No.168, Section 1, University Rd., Minhsiung, 621301 Chiayi, Taiwan*

ABSTRACT

In some steep valleys, flood-induced changes in river bed elevation pose significantly greater risks to infrastructure than floodwaters alone. Over the short term, the river may aggrade or degrade by several meters during a single flood. Whereas floodwaters recede after each event, moreover, riverbed changes add up over successive floods. To quantify the resulting geomorphic risk and its evolution over time, we propose in this paper a new stochastic model of river bed elevation change. The bed is assumed to rise and drop according to a random walk, driven by the composition of two gamma processes that respectively pace the hydrologic forcing and the geomorphic response. The model can therefore incorporate various sources of uncertainty, associated with precipitation and debris flow activity within the contributing watershed. To test the model, we apply it to a highly active montane river, the Laonong River in southwestern Taiwan. Model calibration is achieved from a combination of long and short term data, including radiocarbon-dated deposits and modern river records. The modelled distributions fit the data well, including the likelihood of extreme changes. The model also produces a reasonable hindcast of the geomorphic damage suffered over the last ten years by Highway 20, a vulnerable road link sited along the river, and can be used to forecast future geomorphic risk.

1. Introduction

River floods represent one of the major threats to civil infrastructure. In many cases, floods may not just cause inundation and local scour, but also broader geomorphic changes like channel widening or avulsion, and changes in river bed elevation (Lane, 1955; Bull, 1988; Kochel, 1988). In steep valleys, rivers may undergo little change over long periods, then sudden episodes of rapid aggradation and degradation. Around the world, several such episodes have been documented, in which a single flood has caused the river bed to rise or drop by several meters. Early documented cases include episodes in Taiwan (Lane, 1955), Texas (Baker, 1977), and California (Nolan and Marron, 1985). In recent decades, cases that have been documented in detail include episodes in Canada (Lapointe et al., 1998; Brooks and Lawrence, 1999; Capart et al., 1997), New Zealand (Korup, 2004), La Réunion (Garcin et al., 2005), Taiwan (Hsieh and Capart, 2013), and Switzerland (Turowski et al., 2013; Ruiz-Villanueva et al., 2018).

In many recorded cases, rapid changes in river bed elevation have

threatened or destroyed bridges and roadways (Korup, 2004; Yochum et al., 2017; Hackl et al., 2018; Ruiz-Villanueva et al., 2018; Seier et al., 2020) or other riverine infrastructure like hydropower plants, run-of-the-river dams and diversion weirs (Lane, 1955; Lapointe et al., 1998; Hsieh and Capart, 2013). When aggradation is severe, such assets may directly get buried by the sediments. Aggradation can also indirectly raise flood levels, and reduce the clearance necessary to convey floods. When the trunk river aggrades, moreover, this raises the base level of tributaries, causing debris fan aggradation to reach higher elevations. River bed degradation, on the other hand, can undermine banks and foundations to the point of failure (Lo et al., 2021).

An example of such risks is provided by the Laonong river valley, in southwestern Taiwan, where an exceptional geomorphic flood event due to the 2009 Morakot Typhoon caused multiple bridge failures and the partial destruction of Highway 20, sited along the river (Chien and Kuo, 2011; Yeh, 2012; Lin, 2012). Since then, the reconstructed bridges and roadway continue to be threatened by river bed changes. This is illustrated in Figs. 1 and 2 by the Aqiba bridge site, where three successive

---

bridges have been destroyed or endangered. Before Typhoon Morakot, a low girder bridge and a higher suspension bridge were built across the Laonong river, with bridge decks set 10 and 23 m above the river bed, respectively (Fig. 1a). Due to Typhoon Morakot, the low girder bridge was buried beneath 20 m of river bed aggradation. The higher suspension bridge was destroyed by the same flood, but its tower was left standing and fully exposed (Fig. 1b). Thereafter, further aggradation completely buried the tower, before its top was re-exposed in September 2019 due to river degradation (Fig. 1c). Most recently, in August 2021, the old tower was buried again by renewed aggradation (Fig. 1d). Built after Morakot, a new suspension bridge was set significantly higher (Fig. 1c and d), but the river bed has now risen to within 6.3 m of the bridge deck, and subjected the right abutment to scour damage. The three bridges and their height relative to the evolving river bed elevation are shown on a cross-section of the valley in Fig. 2.

To assess risks in such circumstances, a probabilistic or stochastic approach is needed. For bridge failure due to flood submersion or local scour, probabilistic models have been proposed by Johnson and Dock (1998); Anarde et al. (2018), and Lamb et al. (2019), to quantify failure probability conditional on the severity of a flood event. The floods themselves can often be modelled as independent, identically distributed events, and characterized by an annual exceedance probability. For river bed aggradation and degradation, however, the effects of successive floods typically cause cumulative changes in river bed elevation. To assess the corresponding risks, therefore, a stochastic model capturing the random evolution of the system over time becomes necessary. Such models have been proposed to model sediment supply to channel networks (Benda and Dunne, 1997), episodic coastal cliff retreat (Hall et al., 2002), general processes of erosion and deposition (Schumer et al., 2011), gradual changes in river rating curves (Reitan and Petersen-Øverleir, 2011), and channel width evolution due to flood erosion and vegetation encroachment (Davidson and Eaton, 2018). To our knowledge, so far no such model has been developed or tested to model episodic river bed elevation changes.

In this paper, we propose such a model, describing the time evolution of the river bed elevation as a random walk. To avoid unbounded drift over long times, we model this random walk as a mean-reverting process. To simulate the episodic pace of river bed evolution, we subordinate this process to another random process, which modulates the rate of change. We use this to account, first, for the variability over time of the precipitation experienced by the watershed. Secondly, we want to account for the uncertainty associated with the geomorphic response of the valley (Kochel, 1988; Cenderelli and Wohl, 2003). Specifically, the rate of river bed elevation change may be affected by catchment processes like the supply of sediment by landslides (Korup, 2004; Lin and Lin, 2015; Xiong et al., 2022), debris flows (Capart et al., 2010; Hsieh and Chyi, 2010) or glacier activity (Knox, 1996; Pfeiffer et al., 2019). To include both contributions, we therefore propose to drive the random walk by the composition of two processes that respectively pace the hydrologic forcing and the geomorphic response.

The paper is structured as follows. In Section 2, we describe the components of our proposed model and the key properties of the resulting stochastic process. In Section 3, we describe the Laonong river study area selected to test the model and the collected river data. In Section 4, we use these data to calibrate model parameters and to compare modelled and observed distributions. In Section 5, we use the calibrated model to hindcast past damage and forecast future geomorphic risk to infrastructure in this valley. Finally, conclusions are drawn in Section 6.

2. Stochastic model of river bed evolution

In this paper, we propose to model river bed evolution as a random walk $Z(\tau_g(t))$ [m], where Z is the river bed elevation at a station, t [yr] is the calendar time, and τ_g [yr] is a geomorphic time, governing the pace of geomorphic evolution. As in the Variance Gamma (VG) process proposed by Madan and Seneta (1990) and Madan et al. (1998), we let the time evolution of the variable of interest Z result from the composition of two random processes. The first governs the evolution of Z as a function of τ_g, and allows both rises and drops to account for aggradation and

Fig. 1. Risk to infrastructure due to river bed elevation change, as illustrated by the Laonong River at the Aqiba bridge site: (a) before 2009 (roadside hot spring advertisement); (b) in February 2010, after the Morakot geomorphic flood; (c) in September 2019; (d) in August 2021 (see text for description).

degradation. The second governs the evolution of τ_g with t, where the geomorphic time τ_g advances monotonously with calendar time t, but at a rate that varies randomly over time. We model the first process using the stochastic differential equation (SDE) (Reitan and Petersen-Øverleir, 2011)

$$dZ = \lambda_g(z_\infty - Z)\,d\tau_g + \sigma_g\,dW(\tau_g), \tag{1}$$

where d denotes an infinitesimal increment, and bed elevation increments dZ are obtained as the sum of two terms. The first term, controlled by the reversion rate parameter λ_g [yr^{-1}] represents the tendency of the river bed elevation to revert to its long term mean z_∞ [m]. The second term, controlled by the volatility σ_g [m yr$^{-1/2}$] represents random perturbations modelled by the Wiener process $W(\tau_g)$ [yr$^{1/2}$]. A SDE like Eq. (1) is similar to an ordinary differential equation but evolves in response to random perturbations instead of a deterministic forcing (for an introduction to SDEs, see Øksendal (2000)).

Taken as a function of τ_g, the process described by Eq. (1) is known as the Ornstein–Uhlenbeck (OU) process (Uhlenbeck and Ornstein, 1930). This process is widely used in many areas of physics (Gillespie, 1996), and has been used previously by Reitan and Petersen-Øverleir (2011) to model random river bed evolution as a function of calendar time. Subordinating an OU process to another random process, called the subordinator, to vary the pace of evolution has also been investigated in earlier work (Barndorff-Nielsen and Shepard, 2001; Habtemicael and SenGupta, 2014). In these earlier models, however, a gamma process was used only to drive the Wiener process component of Eq. (1), with mean reversion assumed to proceed according to calendar time.

To model the randomly varying pace of geomorphic evolution, we further propose to describe the process $\tau_g(t)$ as the composition

$$\tau_g(t) = \tau_{gh}(\tau_h(t)), \tag{2}$$

where $\tau_h(t)$ is a hydrologic time, assumed proportional to the cumulative rainfall $R(t)$, and where $\tau_{gh}(\tau_h)$ maps hydrologic time to geomorphic time. The hydrologic time is needed to account for yearly variations in the magnitude of the hydrologic forcing.

For both processes, we assume positive, gamma-distributed increments. For the hydrologic time $\tau_h(t)$, we assume gamma-distributed precipitation (Eagleson, 1978; Martinez-Villalobos and Neelin, 2019), hence increments $\Delta\tau_h = \Delta R/\mu_h \sim \Gamma(\Delta t/\nu_h, \nu_h)$, where μ_h is the mean annual rainfall, $\Delta t/\nu_h$ [-] is the shape parameter and ν_h [y] is the scale parameter of the gamma distribution. As illustrated in Fig. 3a, the gamma process $\tau_h(t)$ results from an accumulation of gamma-distributed increments $\Delta\tau_h$ over successive time increments Δt, and takes the form of an irregular staircase with jumps of random magnitude. The scale

parameter ν_h sets the amplitude of these steps (see the small scale bar on Fig. 3)a and the time intervals between successive steps, hence controls the episodicity of the hydrological forcing. We will therefore call this parameter the *hydrologic episodicity*, for short. In the limit of zero episodicity, a continuous ramp with linear rise would be obtained. In practice, the process $\tau_h(t)$ is simulated using Monte-Carlo simulations. At discrete times t_j, $\tau_{hj} = \sum_{k=1}^{j}\Delta\tau_{hk}$, where $\Delta\tau_{hk} = \Gamma_{hk}(\Delta t_k/\nu_h, \nu_h)$ is a gamma-distributed independent pseudo-random number. In Fig. 3a, we show 30 realizations of $\tau_{hj}(t_j)$ with $\nu_h = 0.5$ yr and $\Delta t = 0.1$ yr.

For the process $\tau_g(\tau_h)$, taken as a function of hydrologic time, we likewise assume gamma-distributed increments $\Delta\tau_g \sim \Gamma(\Delta\tau_h/\nu_{gh}, \nu_{gh})$, where ν_{gh} [yr] is the episodicity of the geomorphic response subject to given hydrologic forcing, or geomorphic response episodicity for short. In Fig. 3b, we show 30 realization of the process $\tau_g(\tau_h)$, as obtained by Monte-Carlo simulations, choosing for the geomorphic response episodicity the larger value $\nu_{gh} = 1$ *yr*. Comparing Fig. 3b with Fig. 3a shows that this greater episodicity produces less frequent jumps of greater magnitude, hence a signal that drifts more quickly away from a proportional rise. The composite process $\tau_g(t) = \tau_{gh}(\tau_h(t))$, finally, is obtained by composing the two gamma processes illustrated in Fig. 3a and b. In Fig. 3c, we show 30 realizations of this composite process, again obtained by Monte-Carlo simulations, using the same values $\nu_h = 0.5$ yr and $\nu_{gh} = 1$ yr for the contributing episodicities. From such simulations, we can observe that the composite process $\tau_g(t) = \tau_{gh}(\tau_h(t))$ is visually indistinguishable from a single gamma process of effective episodicity ν_g given by

$$\nu_g = \nu_h + \nu_{gh}, \tag{3}$$

or simply the sum of the two contributing episodicities. In Appendix A, we provide a mathematical derivation showing that this equivalence, although not exact, holds to a very good approximation.

To complete the model, we let the geomorphic time $\tau_g(t)$ pace the evolution of the SDE defined by Eq. (1). This is done in practice using Monte-Carlo simulations, starting each realization from initial condition z_0, then updating the river bed elevation over successive geomorphic time intervals $\Delta\tau_{gj}$ by using the recursion

$$Z_j = Z_{j-1} + \lambda_g(z_\infty - Z_{j-1})\Delta\tau_{gj} + \sigma_g\Delta W_j, \tag{4}$$

where

$$\Delta W_j = \sqrt{\Delta\tau_{gj}}\,N_j(0,1), \tag{5}$$

and where each $N_j(0,1)$ is a pseudo-random number drawn from a normal distribution of mean 0 and variance 1.
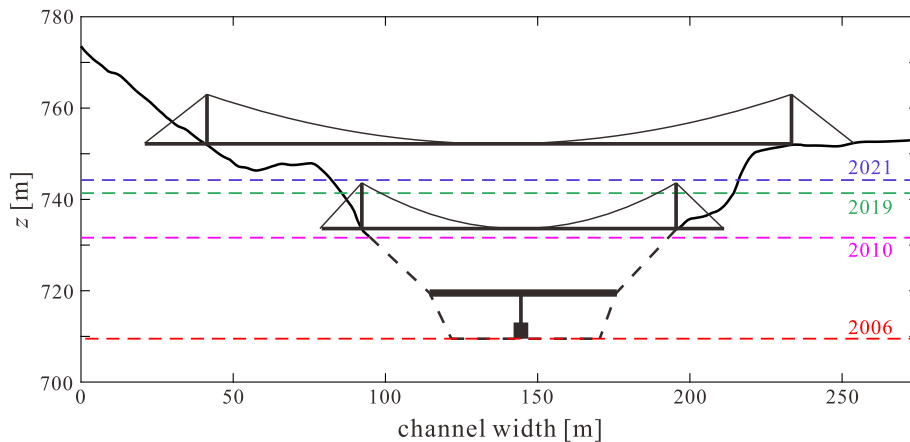

Fig. 2. Cross-section across the Laonong valley at the Aqiba bridge site, showing the current and previous bridges, and successive changes in river bed elevation (dashed lines).
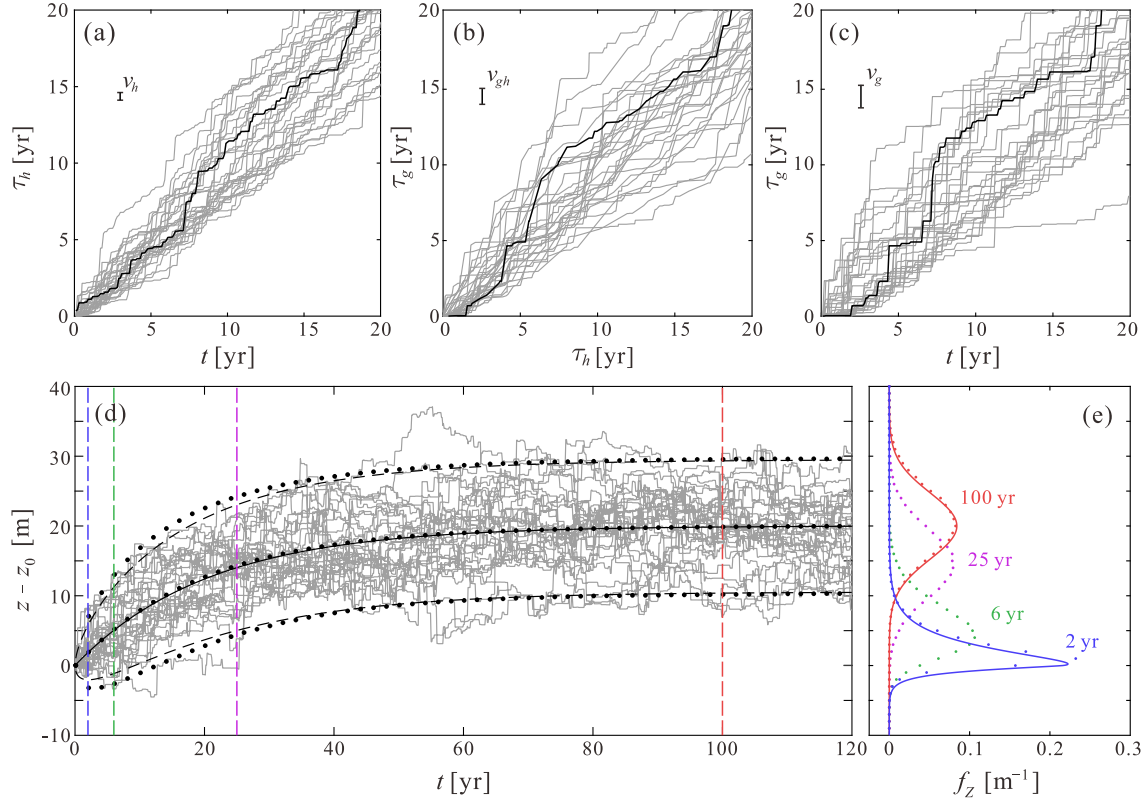
Fig. 3. Monte-Carlo simulations of river bed elevation change assuming hypothetical parameter values $\Delta t = 0.1$ yr, $\lambda_g = 0.05\text{yr}^{-1}$, $z_0 = 0$ m, $z_\infty = 20$ m, $\sigma_g = 1.5$ m/yr$^{1/2}$, $\nu_h = 0.5$ yr, $\nu_{gh} = 1$ yr: (a) 30 sample paths of hydrologic time τ_h as a function of calendar time t; (b) 30 sample paths of geomorphic time τ_g as a function of hydrologic time τ_h; (c) 30 sample paths of the composite process $\tau_g(t) = \tau_{gh}(\tau_h(t))$; (d) 30 bed elevation histories $Z(t)$ (gray lines) and the evolving mean ± 2 standard deviations obtained from $M = 10^5$ MC simulations (dots) and from the approximate formulas Eq. (7) (continuous line) and Eq. (8) (dashes); (e) elevation distribution at different times obtained from $M = 10^5$ MC simulations (dots), and from the approximate short and long time pdfs (solid lines).

The resulting model behavior is illustrated in Fig. 3d, for assumed hypothetical parameter values $\lambda_g = 0.05\text{yr}^{-1}$, $z_\infty - z_0 = 20$ m, $\sigma_g = 1.5$ myr$^{-1/2}$. In Fig. 3d, we show 30 realizations of the process (gray lines), as obtained from Monte Carlo simulations. Over short times, the paths undergo a sequence of sudden rises and drops, causing a cumulative drift. Over long times, however, the paths do not drift away without bounds. After a few decades, they eventually fluctuate around the long term mean with finite variance. Unlike previous models (Barndorff-Nielsen and Shepard, 2001; Habtemicael and SenGupta, 2014), which revert to the mean gradually, here the process does so by way of discontinuous jumps.

The process described above is straightforward to simulate by Monte-Carlo, but difficult to analyze and calibrate due to the influence of multiple parameters. To clarify model behavior and guide the calibration of its parameters, it is therefore useful to consider a simpler, approximate version. for this purpose, we approximate the composite process $\tau_g(t) = \tau_{gh}(\tau_h(t))$ by a single gamma process $\tau(t)$, characterized by increments $\Delta\tau \sim \Gamma(\Delta t/\nu_g, \nu_g)$, of effective episodicity ν_g given by Eq. (3). Subject to this approximation, the river bed evolution $Z(t)$ becomes an Ornstein–Uhlenbeck process $Z(\tau)$ subordinated to the single gamma process $\tau(t)$. This process is governed by the stochastic differential equation

$$dZ = \lambda_g(z_\infty - Z)\,d\tau + \sigma_g\,dW(\tau), \tag{6}$$

where $\tau(t)$ has gamma-distributed increments $\Delta\tau \sim \Gamma(\Delta t/\nu_g, \nu_g)$. Using variation of parameters, we can then derive explicit formulas for the time-evolving mean and variance of this approximate process (detailed derivations are presented in Appendix B). For the time-evolving mean, or expected elevation of the river bed as a function of time, we get

$$\mathbb{E}[Z(t)] = z_0 + (z_\infty - z_0)\left(1 - (\lambda_g\nu_g + 1)^{-t/\nu_g}\right). \tag{7}$$

where $\mathbb{E}$ denotes the expectation operator. The mean gradually transitions from the initial condition z_0 to the long term mean z_∞. Likewise the time-evolving variance reads

$$\text{Var}(Z(t)) = \frac{\sigma_g^2}{2\lambda_g}\left(1 - (2\lambda_g\nu_g + 1)^{-t/\nu_g}\right), \tag{8}$$

which converges asymptotically towards a finite long term variance $\sigma_\infty^2 = \sigma_g^2/2\lambda_g$. The episodicity ν_g does not affect the long term asymptotes, but alters the time evolution of the two moments (the mean and the variance). In the limit as $\nu_g \to 0$, the known formulas for the time-evolving mean and variance of the standard OU process (Gardiner et al., 1985, Chapter 4.4.4) are recovered.

Although the time-evolving mean and variance can be obtained analytically, the corresponding time-evolving probability distribution function (pdf) is beyond our reach. For our field case of interest, however, there is a clear separation between the short time scale governing episodicity, and the long time scale governing mean reversion. Over short times, when Z is still close to z_0, the mean-reversion term can be approximated by a constant drift $\lambda(z_\infty - z_0)\,d\tau$ hence the process of Eq. (6) reduces to the Variance-Gamma (VG) process

$$dZ = \mu_0\,d\tau + \sigma\,dW(\tau), \tag{9}$$

where $\mu_0 = \lambda(z_\infty - z_0)$ is the assumed constant drift rate. The resulting increments ΔZ have the pdf of the VG process, given by (Madan and Seneta, 1990; Brigo et al., 2009)

$$f_{\Delta z_{VG}}(\Delta z | \Delta t) = \frac{2 e^{\mu_0 \Delta z / \sigma_g^2}}{\sqrt{2\pi} \sigma_g \nu_g^{\Delta t / \nu_g} \Gamma(\Delta t / \nu_g)} \left(\frac{|\Delta z|}{\zeta} \right)^{\eta} K_{\eta} \left(\frac{|\Delta z| \zeta}{\sigma_g^2} \right), \qquad (10)$$

where $\zeta = \sqrt{\mu_0^2 + 2\sigma_g / \nu_g}$, $\eta = \Delta t / \nu_g - 1/2$, and $K_{\eta}(\cdot)$ is the modified Bessel function of the second kind with index η. Over long time, the central limit theorem applies and the process approaches the normal distribution with stationary mean z_{∞} and variance σ_{∞}^2. In the next section, we will exploit this property to calibrate parameters sequentially based on long and short term data.

In Fig. 3d and e, we compare the above analytical results with the Monte-Carlo simulations. In Fig. 3d we plot the time-evolving mean (solid line) plus/minus two standard deviations (dashed lines), as calculated using Eqs. (3), (7) and (8). These can be compared with the numerical values calculated from $M = 10^5$ Monte Carlo simulations (dots). This confirms that a single gamma process with aggregate episodicity approximates well the composition of two gamma processes. The analytical results for the approximate model match closely the Monte-Carlo results for the time-evolving mean elevation, but underestimate slightly the corresponding variance at intermediate times.

In Fig. 3e, the time evolution of the pdf is illustrated, allowing us to compare the analytical short and long term pdfs (solid lines) with results from $M = 10^5$ Monte Carlo simulations (dots). At the relatively short time $t = 2$ yr, the simulated pdf (dots) agrees well with the analytical VG distribution given by Eq. (10) (solid line), which features an asymmetric shape and a cusped peak. The simulated pdfs then gradually evolve
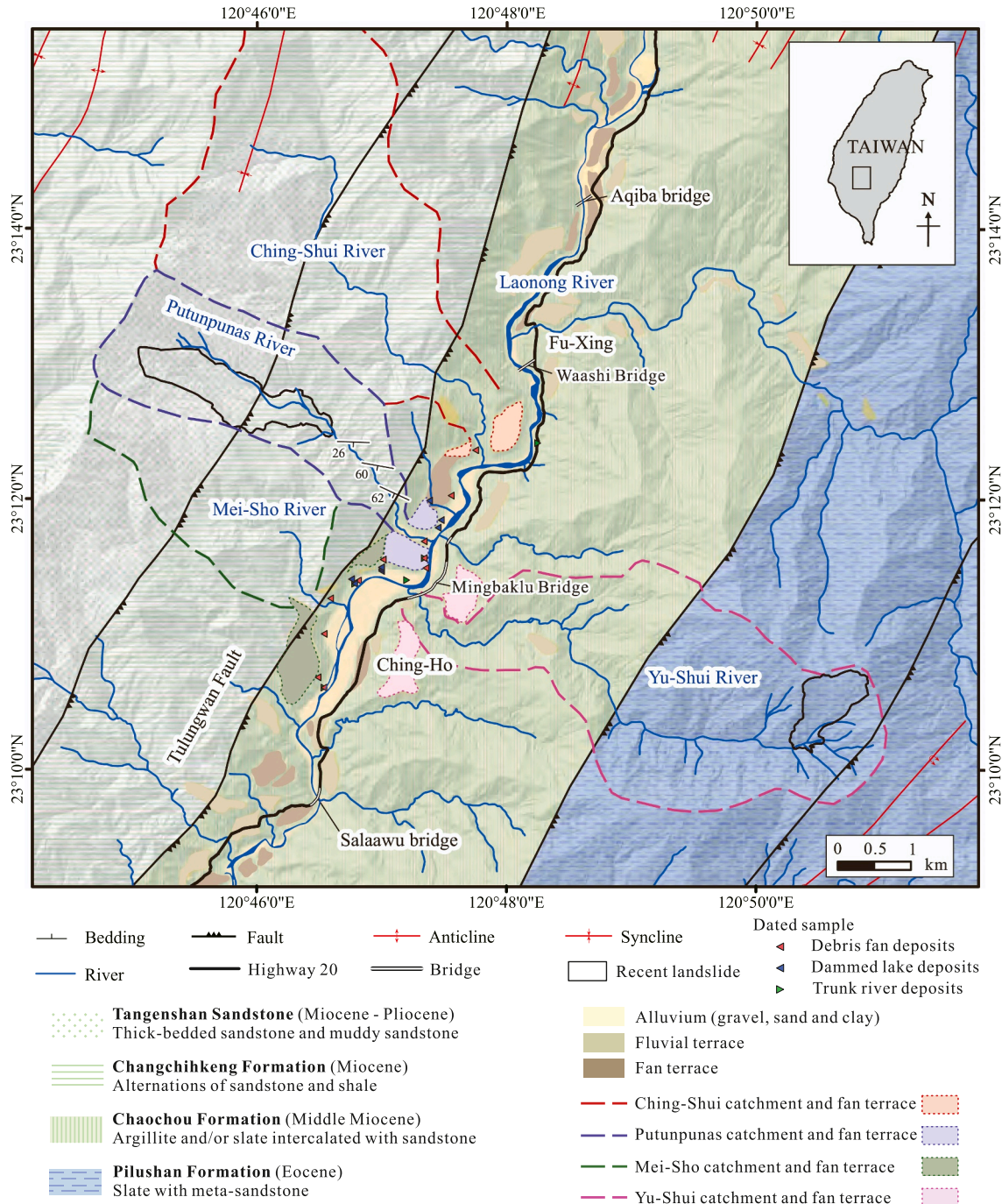

Fig. 4. Geological map of the study area (map credit: Pai-Chiao Lo).

towards the normal distribution. At time $t = 120$ yr, the simulated pdf (dots) nearly coincides with the asymptotic normal distribution $N(z_\infty, \sigma_\infty^2)$ (solid line).

3. Study area and data sources

To test the model, we apply it to the Laonong River, a highly active montane valley located in Southwestern Taiwan (Fig. 4), focusing on the segment extending from Aqiba Bridge to Salaawu Bridge, some 12 km downstream. The regional geological setting is illustrated in Fig. 4. The river drains an elongated, narrow watershed oriented parallel to faults, synclines and anticlines. Both sides of the valley feature steep watersheds prone to landsliding and debris flows, providing an intermittent supply of debris to tributary mouths. This produces the formation of tributary fans that record past and recent episodes of debris supply.

Along the valley segment, four tributaries exhibit elevated terraces built up by debris flows over the past 2000 years (Hsieh and Chyi, 2010; Hsieh and Capart, 2013). From upstream to downstream, they are the Ching-Shui, Putunpunas, Yu-Shui, and Mei-Sho tributaries (Figs. 4 and 5). Their levels of activity have varied significantly over recent decades. On the right side of the valley, the Putunpunas tributary was already moderately active before Morakot Typhoon, and contributed massive volumes of debris both during the typhoon and over the ensuing years (Hsieh and Capart, 2013). The Ching-Shui tributary, previously dormant, was reactivated by Typhoon Morakot to produce a fresh tributary fan. On the left side, the Yu-Shui tributary was less active before, during, and in the first few years following Typhoon Morakot, but produced fresh fan deposits over the last three years (Yang et al., 2022). Finally the Mei-Sho tributary, in spite of its thick ancient terraces, has not delivered significant debris volumes over the last 20 years.

Within each catchment, landslides respond intermittently rather than proportionally to each storm or typhoon. The recent aggradation of the Yu-Shui debris fan, for instance, is associated with the fresh activation of a large landslide within its catchment (Yang et al., 2022). Our proposed stochastic model does not represent such catchment dynamics explicitly, but accounts for their influence on trunk river evolution via the composition (Eq. 2). The supply of debris by different tributaries thus exhibits a lack of synchronicity, despite their forcing by roughly the same precipitation history. Accounting for geomorphic response episodicity in addition to hydrologic episodicity therefore appears necessary to model the response of this valley.

Sited along this valley is an important roadway link, Highway 20, forming part of the southern cross-island highway that connects the western and eastern parts of Taiwan. The road also serves a number of communities along the valley, for which it is a vital transportation link. Due to typhoon Morakot, in August 2009 the highway segment, its bridges and slope-retaining structures were buried by 20 m of trunk river aggradation. The segment was also among the last to be reconstructed after the typhoon, coming back into service only in 2017 with the completion of Minbaklu Bridge (Fig. 5). More recently, in 2021, the roadway was again damaged by the accumulation of fresh fan deposits

at the Yu-Shui confluence (Yang et al., 2022). An oblique aerial view of the valley and Highway 20 soon after this most recent geomorphic episode is shown in Fig. 5.

As illustrated in long profile by Fig. 6, a number of infrastructure assets have been destroyed along this segment due to changes in river bed elevation. In 2007, aggradation helped destroy the 100 m long Hsing-Huei Bridge, by raising the water profile and causing flood waters to push the concrete bridge deck off its lateral and central supports (Capart et al., 2010). In 2009, the record-breaking geomorphic flood due to Typhoon Morakot caused the burial or flood destruction of five bridges across the Laonong River. From upstream to downstream: the Aqiba girder and suspension bridges, the Ching-Shui and Shao-Nian suspension bridges, and the Salaawu girder bridge. River aggradation also buried the site of a weir and tunnel entrance then under construction on the right side of the valley (Hsieh and Capart, 2013).

For this valley segment, the data available for model calibration are unusually complete (see Table 1). First, two sets of river elevation data can be exploited: radiocarbon-dated terrace deposits, for the long term, and modern river elevation records, for the short term. Along the segment, multiple wood and vegetation fragments collected from exposed fluvial and debris flow sequences were radiocarbon-dated, and their elevations registered relative to the river long profile (Hsieh and Chyi, 2010; Hsieh and Capart, 2013). The locations in plan are illustrated in Fig. 4, and we also show the locations, elevations, and dates (x_i, z_i, t_i) of these dated deposits in profile in Fig. 6. The deposits from gravelly debris fan, sandy dammed-lake, and gravelly trunk river are labeled as red, blue, and green triangles, respectively. As illustrated in Fig. 7a, they provide a record of the river elevation changes experienced by the valley over the last two millennia and indicate that, over this period, the Laonong river underwent multiple episodes of rapid aggradation and degradation, including changes of even greater magnitude than the 2009 Morakot event. Knox (1996) likewise used radiocarbon-dated deposits to reconstruct past alluvial episodes along the Upper Mississipi River.

Among these dated deposits, trunk river deposits (green bars) were preserved only near the bottom of the valley. Tributary debris fan (red bars) and dammed lake deposits (blue bars), however, could be identified over a wide range of elevations. Since their elevations approximate the trunk river elevation at the time of deposit, we will use them as proxies for past river bed elevations. No samples could be collected below the lowest profile attained by the river over the period of data collection, hence this record is truncated at the elevation of the 2008 river bed. The 19 dated tributary debris fan and dammed lake deposit records are sparse, and their dates uncertain, hence they do not accurately resolve river elevation fluctuations over short time scales. They do, however, provide an approximately random sample of the river bed elevations experienced over a long time period.

To document more recent river elevation changes, we compiled all the river bed elevation data available to us at the Aqiba Bridge site (Fig. 8a). At this site, a gauging station operated by the Taiwan Water Resources Agency (WRA) acquired detailed records of river bed

Fig. 5. Composite aerial view of the valley segment showing tributaries, Highway 20 and the along-river Minbaklu Bridge after the most recent episode of river aggradation in August 2021.
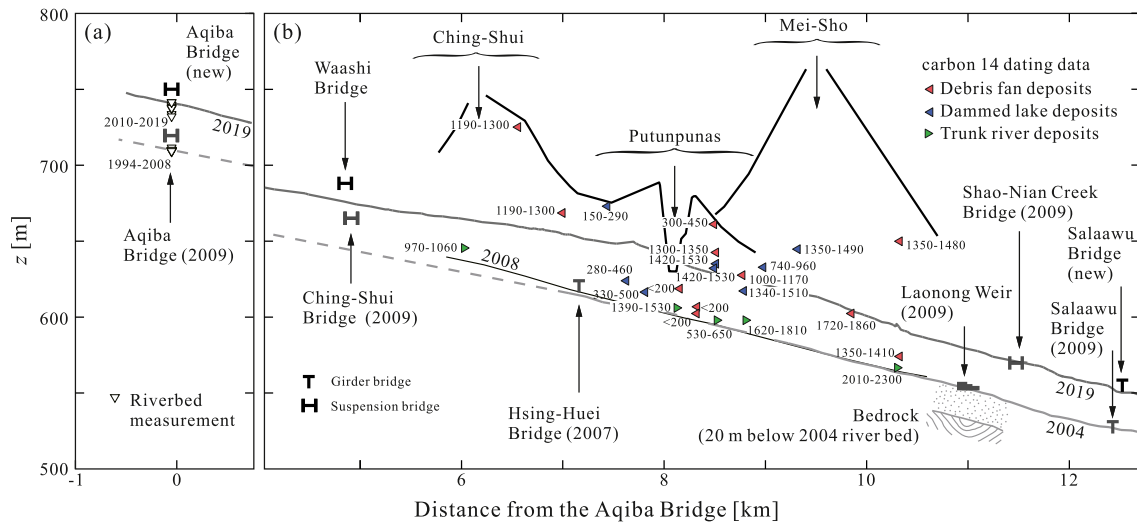
Fig. 6. Engineered structures and dated deposits along a segment of the Laonong river valley, shown relative to long river profiles and to truncated debris fans. A date in parentheses indicates the year of destruction of a structure. Dated sample: Debris fan deposits (red triangle), dammed lake deposits (blue triangle), and trunk river deposits (green triangle).

Table 1
Model calibration data.

Data	Period	No. of data	Source
Dated deposit heights y	2500–0 cal. BP	19	Hsieh and Capart (2013)
River elevation records ΔZ	1994–2019	25	WRA
Annual rainfall ΔR	1994–2019	25	WRA

elevations over periods 1994–2009 and 2014–2017. This station was destroyed by Typhoon Morakot in 2009, and rebuilt in 2014. We supplement these data with elevations estimated from site photos, in 2010, 2012, and 2013, and with elevations acquired by topographic survey in 2018 and 2019. To estimate the hydrological forcing experienced by the valley, finally, we have at our disposal the daily rainfall data acquired by the WRA at the Tian-Chi rain gauge over the period 1994–2019.

4. Model calibration and comparison

To apply our proposed stochastic model to the Laonong valley segment described in the previous section, it is necessary to calibrate

seven distinct model parameters, listed in Table 2. Four of these parameters can be calibrated from recorded river elevation changes alone: the long-term mean z_∞, the reversion rate parameter λ_g, the volatility σ_g, and the geomorphic episodicity ν_g. Two parameters can be determined from hydrological records alone: the hydrological episodicity ν_h and mean annual rainfall μ_h. Finally a combination of river and rainfall records is needed to calibrate the geomorphic response episodicity ν_{gh}.

Taking advantage of the separation of scale property described in the previous section, the radiocarbon-dated records allow calibration of the mean z_∞ and variance $\sigma_\infty^2 = \sigma_g^2/(2\lambda_g)$ of the long time stationary pdf. For this purpose, we take as observed data the dated deposit elevations $\mathbf{y} = \{y_1, ..., y_N\}$ relative to the 2008 river profile, where $y_i = z_i - z_{2008}(x_i)$. To account for the truncation of these data below elevation z_{2008} ($y = 0$), we adopt the modified likelihood function (Hald, 1949)

$$L(\mathbf{y};\theta) = \prod_{i=1}^{N} \frac{f(y_i;\theta)}{1 - F(0;\theta)}, \tag{11}$$

where $\theta = (z_\infty, \sigma_\infty)$, F is the cdf, and f is the pdf of the normal distribution. Maximum likelihood estimation (MLE) then yields the estimates $z_\infty = z_{2008} + 22.4$ m and $\sigma_\infty = 35.4$ m. In Fig. 7b, the re-scaled cdf $(F(y) - F(0))/(1 - F(0))$ (line) is plotted against the empirical cdf (circle). This is set equal to $(i - 0.5)/N$ where i is the rank of the i-th observed
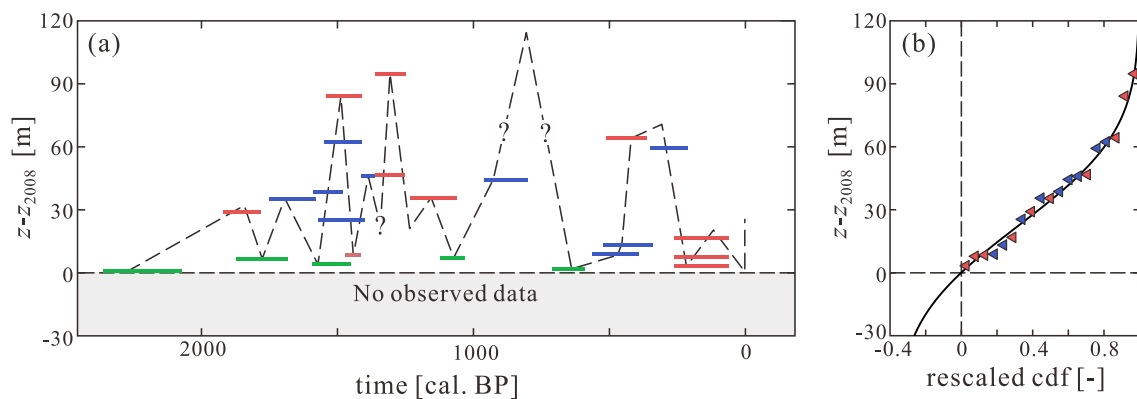

Fig. 7. Model calibration from radiocarbon-dated deposits: (a) river elevation record over the last two millennia deduced from dated trunk river (green bars), tributary debris fan (red bars) and dammed lake deposits (blue bars), with bar widths indicating date uncertainties and the dashed line a tentative reconstruction considering deposit thickness Hsieh and Chyi (2010); Hsieh and Capart, 2013; (b) calibrated (lines) and empirical (circles) long term elevation distributions.
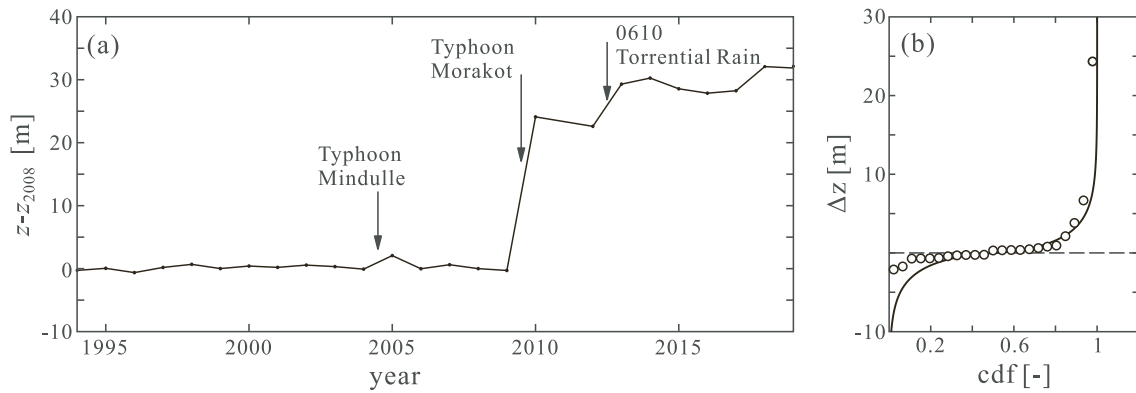
Fig. 8. Model calibration from river elevation records; (a) river bed elevation at Aqiba Bridge since 1994; (b) calibrated distributions (lines) and field data (circles) for the yearly change in elevation.

Table 2
Calibrated model parameters.

Parameter	Calibrated value	Data	Fitted distribution
$z_\infty - z_{2008}$	22.4 m	y	Truncated normal
σ_∞	35.4 m		
μ_0	0.029 m/yr	ΔZ	Variance-Gamma
ν_g	2.38 yr		
μ_h	3691 mm	ΔR	Gamma
ν_h	0.08 yr		
ν_{gh}	2.24 yr	ΔR and ΔZ	Gamma

data, sorted in ascending order. As seen from the comparison, the truncated normal distribution fits the observed data relatively well.

Once the long time behavior has been determined, the parameters governing the short time behavior can be calibrated from the recent river elevation data recorded at the Aqiba bridge site (Fig. 8a). As described in the previous section, the short term evolution of the river bed elevation can be approximated as a Variance Gamma process, whereby the yearly changes ΔZ have the pdf given by Eq. (10). The unknown parameters of this distribution can therefore be determined by MLE from the recorded yearly changes Δz_i. In this procedure, we constrain parameters so that they match the long term stationary distribution determined earlier. This is done by setting the volatility to value $\sigma_g = \sqrt{2\lambda_g}\sigma_\infty$ and the mean reversion rate to value $\lambda_g = \mu_0/(z_\infty - z_0)$, where $z_0 = (z_{1994} + z_{2019})/2$. Thus only two free parameters remain to be calibrated: the initial drift rate μ_0, and the geomorphic episodicity ν_g, for which MLE yields the values $\mu_0 = 0.029$ m/yr and $\nu_g = 2.38$ yr. For the constrained parameters, the corresponding values are $\sigma_g = 3.33$ m/yr$^{1/2}$ and $\lambda_g = 0.0044$yr^{-1}. In Fig. 8b, we compare the cdf calibrated in this way (line) with the empirical cdf (circles).

Over the short term, the observations exhibit a strong bias towards aggradation, with the rises having greater magnitude than the drops. Since the river started off significantly lower than the long term mean elevation z_∞, the model also exhibits this bias, but not as strongly. For aggradation, the modelled distribution matches well the observations, featuring frequent small changes ($0 \leqslant \Delta z < 1$ m), and occasional episodes of moderate ($1 \leqslant \Delta z < 10$ m) to extreme aggradation ($\Delta z \geqslant 10$ m). For degradation ($\Delta z < 0$), on the other hand, moderate river elevation drops ($-10 \leqslant \Delta z < 1$ m) are more frequent in the modelled distribution than in the recently measured record. Over the long term (see Fig. 7a), aggradation and degradation must balance out, hence this under-representation of degradation episodes may be due to the limited duration of the recent record. Alternatively, it may indicate a persistence of the direction of change (aggradation or degradation) over a certain time scale, an effect that is not included in our model. Overall, the modelled distribution fits the data well, including the likelihood of extreme changes, which do not have to be treated as outliers as would be

the case if a Gaussian distribution were assumed. Over short time scales, episodicity must be included to reproduce the observed behavior.

To characterize the hydrologic forcing independently from the geomorphic response, the corresponding model parameters can be calibrated directly from rainfall data. For this purpose, we use the daily rainfall data at the Tian-Chi rain gauge reported by the WRA for the period 1994–2019. Fig. 9a shows the corresponding cumulative rainfall record $R(t)$. To avoid complications associated with seasonality, we use annual rainfall data to calibrate the gamma process representing the hydrologic forcing. This is done by fitting the gamma distribution $\Gamma(1/\nu_h, \nu_h \mu_h)$ to the 26 annual totals ΔR, yielding the values $\mu_h = 3691$ mm/yr for the mean annual rainfall and $\nu_h = 0.08$ yr for the hydrologic episodicity. In Fig. 9b we plot the calibrated cdf (line) against the empirical cdf (circles). From the comparison, it can be seen that the gamma distribution fits the observed annual rainfall data rather well.

Using the approximate additivity property of Eq. (3), we can deduce for the geomorphic response episodicity the value $\nu_{gh} = \nu_g - \nu_h = 2.30$ yr. For comparison, we can also estimate the geomorphic response episodicity by looking at yearly bed elevation changes Δz dependent on the actual annual rainfall ΔR recorded the same year. This provides data pairs $(\Delta\tau_h, \Delta z) = (\Delta R/\mu_h, \Delta z)$, in which the calendar time t is replaced by the hydrologic time τ_h. Over the short term, the conditional distribution $f_{\Delta Z_{VG}}(\Delta z | \Delta\tau_h)$ is again a Variance Gamma pdf, the parameters of which can be estimated by MLE in the same way as before. This alternative procedure yields for the geomorphic response episodicity the slightly smaller value $\nu_{gh} = 2.24$ yr. Although small, the difference between the two values is of the same order as the hydrologic episodicity ν_h. This may indicate more complex interactions between hydrologic forcing and geomorphic response than can be described by the simple composition $\tau_{gh}(\tau_h(t))$ assumed in Eq. (2).

Regardless of how it is estimated, the geomorphic response episodicity ν_{gh} is found to be approximately 20 times greater than the hydrologic episodicity $\nu_h = 0.08$ yr. It therefore makes the dominant contribution to the geomorphic episodicity ν_g. This is also manifest from a visual comparison between Figs. 8 and 9. Comparing Figs. 8a and 9a, we can see that the evolution of the river bed elevation is much more episodic than the evolution of the cumulative rainfall over the same time period. Episodes of strong aggradation, like those produced by Typhoon Mindulle in 2004, Typhoon Morakot in 2009, and the June 10 torrential rain event of 2012, are indeed associated with intense rainfall. However other rainfall events of similar intensity did not produce commensurate geomorphic responses. Taken on a yearly basis, moreover, the rainfall totals experienced by the watershed and the corresponding river elevation changes show strikingly different distributions. Whereas the annual rainfall distribution of Fig. 9b features an elongated body but short tails, the river bed change distribution of Fig. 8b features a compact body (for most years $|\Delta z| < 1$ m) but very long tails, associated
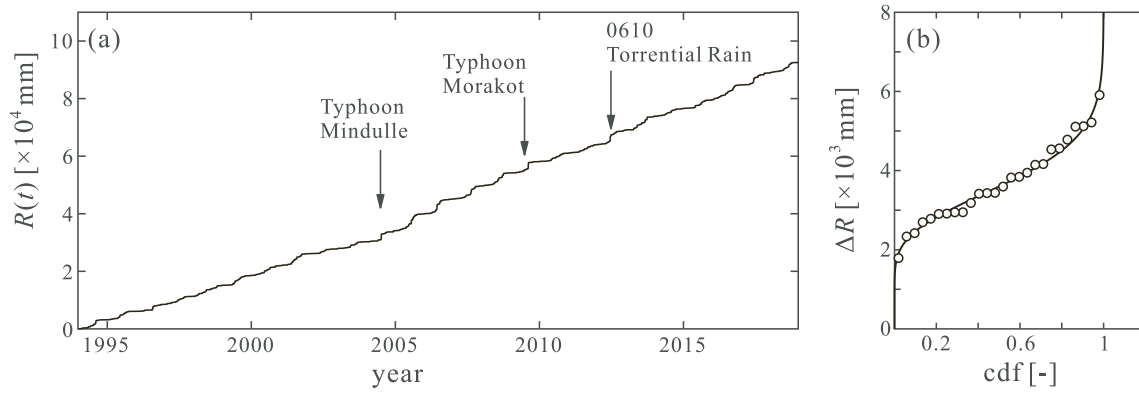
Fig. 9. Model calibration from precipitation data; (a) cumulative rainfall at Tian-Chi rain gauge since 1994; (b) calibrated distributions (lines) and field data (circles) for the annual rainfall.

with infrequent extreme events like the exceptional aggradation episode $\Delta z = 24$ m associated with Typhoon Morakot. To facilitate reference, all the calibrated model parameters are listed in Table 2.

5. Application to risk assessment

Once calibrated, as described in the previous section, our stochastic model can be applied as follows to assess risks to riverine infrastructure. Starting from some initial river profile z_0 at initial time t_0, we can evaluate the probability $P_E^+(z, T)$ that the randomly evolving river bed

elevation $Z(t)$ will exceed elevation z at least once over some planning horizon T:

$$P_E^+(z, T) = P\{\max(Z(t)) \geqslant z, t_0 \leqslant t \leqslant t_0 + T\}. \tag{12}$$

This exceedance probability, therefore, measures the risk that river aggradation will bury an asset (say a roadway or bridge deck) of elevation z during the time period T. Likewise, we can evaluate the probability $P_E^-(z, T)$ that the river bed elevation will drop below level z at least once over the planning horizon T:
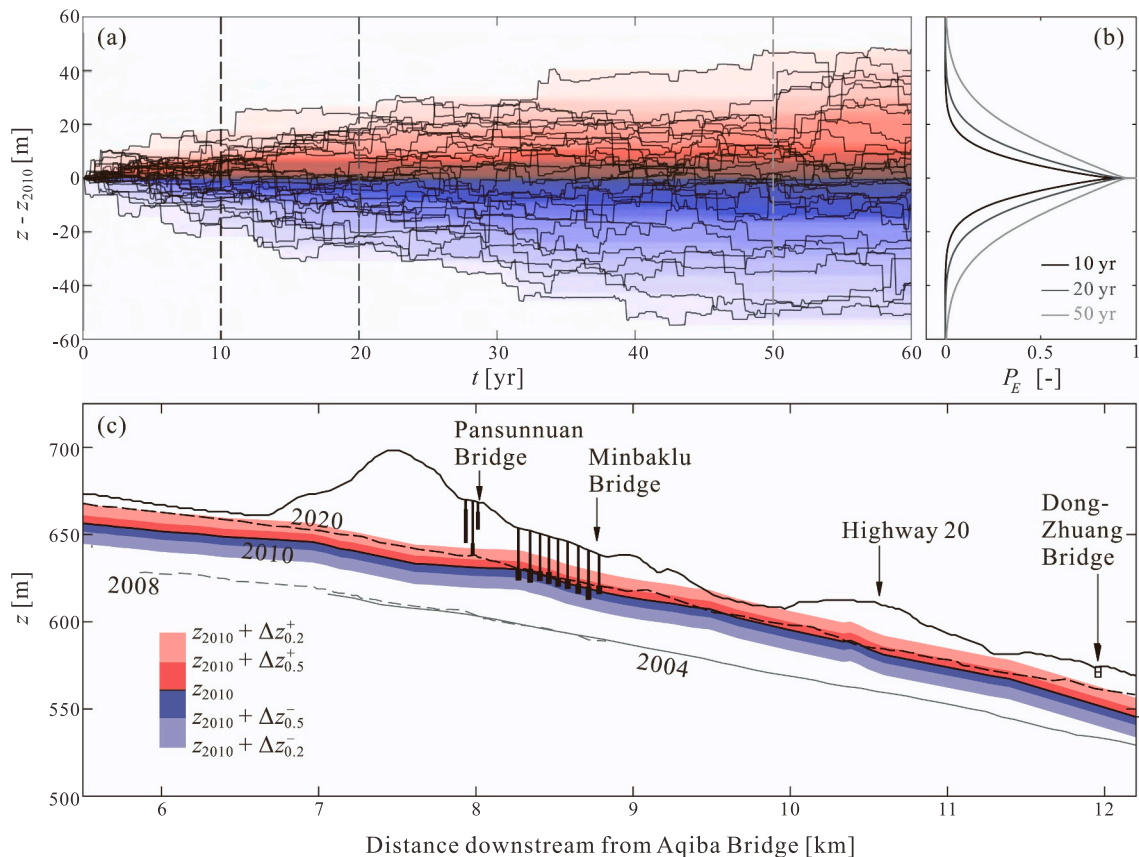

Fig. 10. Hindcast of bed elevation change and infrastructure damage along the Laonong River, for planning horizon 2010–2020: (a) stochastic river bed elevation histories (black lines) and exceedance probability $P_E^+(z, T)$ (red) and $P_E^-(z, T)$ (blue) obtained by 30 Monte-Carlo simulations; (b) exceedance probability as a function of relative elevation for different time horizons, from $M = 10^5$ Monte-Carlo simulations of the calibrated stochastic model; (c) long profiles of the river and road, showing the hindcasted elevation range at risk of aggradation (red) and degradation (blue) over period 2010–2020, for risk levels (probability of exceedance) $P_E = 0.2$ and 0.5 (light and dark bands).

$$P_E^-(z,T) = P\{\min(Z(t)) \leqslant z, \ t_0 \leqslant t \leqslant t_0 + T\}. \tag{13}$$

This measures the risk that river degradation will expose or undermine a foundation element (say a pile cap or caisson base) set at elevation z during the time period T. Over a given time horizon, aggradation risk to a certain asset will depend on the relative height of its superstructure. Likewise, degradation risk will depend on the relative depth of its substructure. In practice, the probabilities P_E^+ and P_E^- can be calculated by running a large number of Monte-Carlo simulations, and evaluating the proportion of realizations meeting the conditions defined by Eqs. (12) and (13). Below we demonstrate this approach by assessing the geomorphic risk incurred by Highway 20 along the Laonong river segment going from Ching-Ho to Fu-Xing, and described earlier in Section 3.

To check that the approach gives reasonable results, we first produce a hindcast, starting from the known river bed elevation in 2010 and calculating the aggradation and degradation risk incurred by Highway 20 over the 10 year period from 2010 to 2020. This can then be compared to the actual river elevation change and highway damage observed over the last 10 years. Fig. 10 shows the simulation steps and the resulting calculated risk levels. In Fig. 10a, we show 30 sample paths (black lines) generated by Monte-Carlo simulation, and their contribution to the aggradation (in red) and degradation risk (in blue) over time. As can be seen from the figure, each time the simulated river bed level exceeds a certain elevation z for the first time, this produces an increment in the probability P_E^+ at this elevation z, over all ensuing times t. Likewise each time the simulated river bed level drops below a certain elevation z for the first time, this produces an increment in the probability P_E^- at this elevation z, over all ensuing times t.

By taking cross sections through this evolving probability distribution, we can obtain profiles of the elevation-dependent risk $P_E^\pm(z)$ over time horizons of interest, for instance 10, 20 and 50 years, as shown on Fig. 10b. To obtain these profiles, we conduct a larger number of Monte-Carlo runs ($M = 10^5$), producing smooth exceedance probability curves. Over time, it is clear that the risk of either aggradation or degradation at a certain elevation can only increase, hence the probability curves gradually diffuse up and down, as illustrated in Fig. 10b. Along the segment considered, the 2010 river long profile is on average 25.6 m higher than it was in 2008 prior to Typhoon Morakot. This is close to the long term mean elevation $z_\infty = z_{2008} + 22.4$ m estimated from the dated deposits. Starting from the 2010 profile, therefore, the mean-reverting term of the model is weak, and the risk curves for aggradation and degradation in Fig. 10b are nearly symmetric. Because river elevation changes are cumulative, the elevation range over which infrastructure is at risk depends strongly on the time horizon. A bridge deck positioned 20 m above the river bed, for instance, will be buried with probability $P_E^+ = 0.040$ over time horizon $T = 10$ yr, but the risk increases to $P_E^+ = 0.13$ over time horizon $T = 20$ yr, and to $P_E^+ = 0.32$ for $T = 50$ yr. This represents a greater increase than if risk were like flood risk, with an annual exceedance probability independent from year to year, in which case we would have $P_E(T) = 1 - (1 - P_E(1))^T$.

To check that the simulations produce reasonable results, in Fig. 10c, we show simulated risk bands over time horizon $T = 10$ yr, calculated using the 2010 river profile as initial condition. On the same long profile, we also show the roadway, bridges and bridge pile foundations of Highway 20, illustrating their location-dependent vulnerability due to differences in relative elevation with respect to the river bed. In 2020, we conducted a new survey of the river long profile, shown in Fig. 10c together with the roadway profile and the river profiles surveyed earlier. We can therefore compare the actual changes experienced by the river from 2010 to 2020 with those expected from the model. For this purpose, we use the curves of Fig. 10b to determine the rise $\Delta z_P^+(T)$ and drop $\Delta z_P^-(T)$ associated with risk level P over horizon T, and add these relative elevations to the initial long profile to determine risk bands. To test whether our stochastic model would have provided a reasonable

assessment of risk over horizon $T = 10$ yr, we can then compare the resulting bands to the actual profile changes, and to the actual damage done to Highway 20 since 2010. This is illustrated in Fig. 10c, using red and blue bands to represent rises and drops, respectively, associated with risk levels $P_E = 0.5$ and 0.2.

As seen on Fig. 10c, the actual elevation changes observed between 2010 and 2020 are consistent with this envelope. Upstream and downstream, the trunk river approximately aggraded up to the $\Delta z_{0.2}^+$ level. In the middle, the profile instead remained with the $P_E = 0.5$ band. Starting from the 2010 profile, the model identifies two low segments of Highway 20 as vulnerable to damage due to trunk river aggradation over a 10 year horizon, and these segments did indeed experience such damage over the ensuing decade. The segment upstream of the Putunpunas confluence has been flooded repeatedly in recent years, which would not have occurred had the river not aggraded between 2010 and 2020. Downstream of the Putunpunas confluence, on the other hand, aggradation along the left bank caused the roadway to be partially buried. The model therefore shows potential as a tool to assess geomorphic risks to roadways and other infrastructure, in this and similar valleys. To evaluate risk more precisely, one would need to consider the local influence of tributary debris fans (Lei et al., 2022). In August 2021, for instance, local aggradation of the Yu-Shui debris fan contributed to the destruction and burial of the downstream spans of Minbaklu Bridge (Yang et al., 2022).

Finally, we can use the model to forecast the risk of future aggradation and degradation along the segment. For this purpose, we again conduct $M = 10^5$ Monte-Carlo simulations, taking the river elevation profile we surveyed in early 2022 as initial condition. The predicted results are illustrated in Fig. 11, using red and blue bands to represent rises and drops, respectively, associated with risk levels $P_E = 0.5$ over different time horizons T. As seen on Fig. 11, over a 10 year horizon, the model identifies two low segments of Highway 20 (the downstream of the Ching-Shui confluence and upstream of the Mei-Sho confluence) as vulnerable to damage due to trunk river aggradation. Over a 20 year horizon, the first vulnerable segment expands to the upstream of the Ching-Shui confluence. Besides, a pile of the Pansunnuan Bridge becomes exposed to failure risk due to trunk river degradation. Further extending to a 50 year horizon, the Highway 20 between the Putunpunas and Mei-Sho tributary confluences, including the Minbaklu Bridge, and the segment near Ching-Ho Village and the Dong-Zhuang tributary confluence also become subject to a high risk of aggradation damage. There is also a high risk that the foundations of Minbaklu bridge will become exposed and undermined due to trunk river degradation.

From the forecast, we can also note a very significant risk that trunk river aggradation will affect the town of Ching-Ho. Over a 50 year horizon, our calibrated model indicates that it is as likely than not ($P_E^+ = 0.5$) that trunk river aggradation will rise up to the level of the lower houses of the settlement. Over shorter time horizons, the probability that river aggradation could rise up to this level is not quite as high, but the risk remains significant. Over time horizons $T = 5$, 10, and 20 years, respectively, we calculate risk levels $P_E^+ = 0.05$, 0.14, and 0.29. As this could entail a significant threat to lives and livelihoods, a more complete assessment of aggradation and flood risk to Ching-Ho and other towns of low elevation relative to the current Laonong river bed (like the town of Fu-Xing not far upstream) is recommended as a high priority.

6. Conclusions

In this paper, we proposed a new stochastic model of river bed elevation changes in steep valleys. Building on previous work, the model lets the bed rise and drop according to a random walk, taking both mean reversion and episodicity into account. To avoid unbounded drift over long times, the walk was described as a mean-reverting Ornstein–Uhlenbeck process. To account for short term episodicity, the OU process was driven by another random process, or subordinator, con-
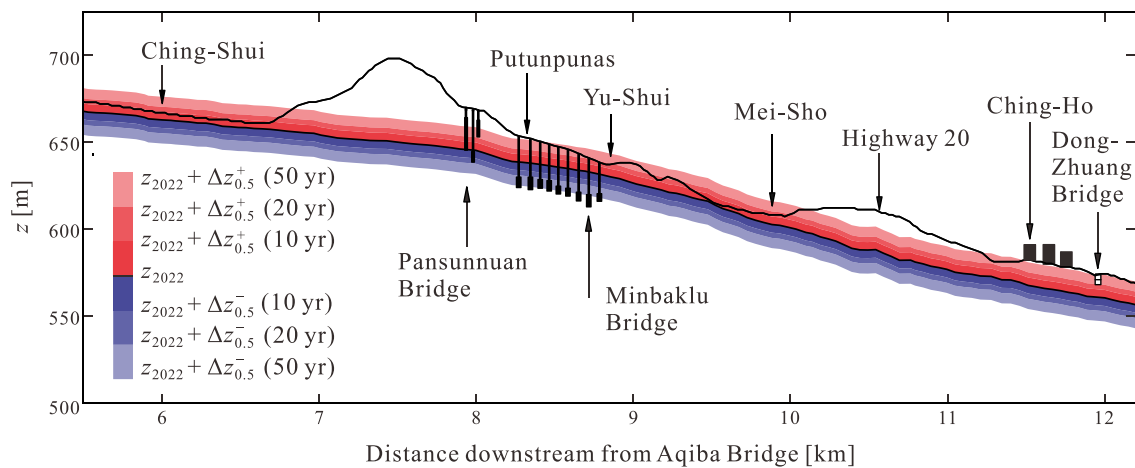
Fig. 11. Risk prediction in next 10, 20 and 50 years. Long profiles of the river bed and road in 2022, showing the forecasted elevation range at risk of aggradation (red) and degradation (blue) in the next 10, 20 and 50 years, for risk levels (probability of exceedance) $P_E = 0.5$.

trolling the pace of evolution. To resolve separately the contributions of hydrologic forcing and geomorphic response, this subordinator was taken as the composition of two gamma processes. In the resulting model, the evolution $Z(t)$ of the bed elevation as a function of calendar time t is described as a composite random process $Z(\tau_g(\tau_h(t)))$, where τ_g is a geomorphic time and τ_h a hydrologic time.

This model was shown to exhibit useful mathematical properties, that clarify its behavior and facilitate parameter calibration. First, the composition of two gamma processes can be approximated by a single gamma process, with episodicity equal to the sum of the contributing episodicities. For the resulting approximate process, we could next obtain the time-evolving mean and variance, and derive probability distribution functions for the short and long time limits. Monte-Carlo simulations were used to check these approximations, and calculate results for the complete version of the model.

Applied to the Laonong River, southwestern Taiwan, the model was found to fit well observed distributions of river bed elevations and elevation changes. Over the long term, mean reversion lets the model converge to a stationary distribution, consistent with the large but finite range of river elevation variation deduced from dated deposits. By accounting for episodicity, the model can also reproduce the compact body and long tails of the short term river bed changes derived from gauge records. By combining river and rainfall data, it was found possible to estimate the relative contributions of hydrologic and geomorphic factors to the variable pace of river bed change. The geomorphic response was found to be much more episodic than the hydrologic forcing, indicating that catchment processes play an important role. The model was also found to produce a reasonable hindcast of the geomorphic damage suffered over the last ten years by Highway 20. Finally, we showed how the model can be used to forecast future risks to riverine infrastructure due to trunk river aggradation and degradation.

Nevertheless, the proposed model is subject to various limitations. First, it does not yield an explicit time-evolving pdf for intermediate times. Second, it does not allow for the possible persistence over time of the tendency of the river bed to aggrade or degrade. Third, it does not yet consider the influence of river bed level rise on flood water levels or bank erosion risk. Finally, it does not resolve longitudinal variations of the river long profile, nor the local influence of debris influx at tributary confluences. Addressing these limitations would allow more precise risk assessment, and are suggested as avenues for future work.

Data availability

The carbon dating data used for model calibration are included in

Hsieh and Capart (2013). Access to the river elevation and rainfall data, and to the Matlab code used to calibrate and apply the model is provided at Zenodo via (https://doi.org/10.5281/zenodo.5731490).

CRediT authorship contribution statement

Declaration of Competing Interest

The authors declare that they have no known competing financial interests or personal relationships that could have appeared to influence the work reported in this paper.

Data availability

Access to the river elevation and rainfall data, and to the Matlab code used to calibrate and apply the model is provided at Zenodo via (https://doi.org/10.5281/zenodo.5731490).

Acknowledgments

Appendix A. Additivity of contributing episodicities

In this appendix, we present an analytical derivation demonstrating that the composition of two gamma processes can be approximated by a single gamma process with additive episodicities. Our goal is to show that the single process $\tau(t)$ of episodicity $\nu_g = \nu_h + \nu_{gh}$ has approximately the same distribution as the composite process $\tau_{gh}(\tau_h(t))$, with contributing episodicities ν_h and ν_{gh}. We will establish this by using moment-generating functions (MGF) and their logarithms, called cumulant-generating functions (CGF). It is known (Stirzaker, 1999) that if two random variables share the same MGF or the same CGF, then they share the same distribution. In our case, the composite and single processes are not identical, but we will show that their CGFs match to a close approximation.

For a random variable X that is gamma-distributed with shape α and scale β, the moment-generating function of X, denoted by M_X, is (Stirzaker, 1999)

$$M_X(u) = \mathbb{E}[e^{uX}] = (1 - \beta u)^{-\alpha}, \tag{A.1}$$

where u is the function variable. The cumulant-generating function of X, denoted by K_X, is the natural logarithm of its moment generating function (Stirzaker, 1999). Therefore,

$$K_X(u) = \log(M_X(u)) = \log\mathbb{E}[e^{uX}] = -\alpha\log(1 - \beta u). \tag{A.2}$$

For $\Delta\tau_g \sim \Gamma(\Delta\tau_h/\nu_{gh}, \nu_{gh})$, we have the moment-generating function

$$M_{\Delta\tau_g}(u) = \mathbb{E}\left\{ \left(1 - \nu_{gh}u \right)^{-\Delta\tau_h/\nu_{gh}} \right\}, \tag{A.3}$$

which can be rewritten

$$M_{\Delta\tau_g}(u) = \mathbb{E}\left\{ \exp\left(\frac{\Delta\tau_h}{\nu_{gh}} \log\left(\frac{1}{1 - \nu_{gh}u} \right) \right) \right\}. \tag{A.4}$$

Let $\log\left(1/(1 - \nu_{gh}u)\right)$ be the function variable, Eq. (A.4) is also the moment-generating function of the random variable $\Delta\tau_h/\nu_{gh}$, which has a gamma distribution with shape $\Delta t/\nu_h$ and scale ν_h/ν_{gh}. Therefore,

$$M_{\Delta\tau_g}(u) = M_{\Delta\tau_h/\nu_{gh}}\left(\log\left(\frac{1}{1 - \nu_{gh}u} \right) \right) = \left(1 - \frac{\nu_h}{\nu_{gh}}\log\left(\frac{1}{1 - \nu_{gh}u} \right) \right)^{-\Delta t/\nu_h}. \tag{A.5}$$

Taking the natural logarithm of this moment-generating function, the cumulant-generating function of $\Delta\tau_g$ can be obtained and expanded into the Taylor series

$$\begin{aligned} K_{\Delta\tau_g}(u) &= \log(M_{\Delta\tau_g}(u)) = -\frac{\Delta t}{\nu_h}\log\left(1 - \frac{\nu_h}{\nu_{gh}}\log\left(\frac{1}{1 - \nu_{gh}u} \right) \right) \\ &= \Delta t\left(u + \frac{1}{2}u^2(\nu_h + \nu_{gh}) + \frac{1}{6}u^3(2\nu_h^2 + 3\nu_h\nu_{gh} + 2\nu_{gh}^2) + \ldots \right). \end{aligned} \tag{A.6}$$

On the other hand, based on Eq. (A.2), a gamma-distributed random variable $\Delta\tau \sim \Gamma(\Delta t/(\nu_h + \nu_{gh}), \nu_h + \nu_{gh})$ has the cumulant-generating function

$$K_{\Delta\tau}(u) = -\frac{\Delta t}{\nu_h + \nu_{gh}}\log\left(1 - (\nu_h + \nu_{gh})u \right), \tag{A.7}$$

which can be expanded into the Taylor series

$$\begin{aligned} K_{\Delta\tau}(u) &= \frac{\Delta t}{\nu_h + \nu_{gh}}\sum_{n=1}^{\infty} \frac{((\nu_h + \nu_{gh})u)^n}{n!} \\ &= \Delta t\left(u + \frac{1}{2}u^2(\nu_h + \nu_{gh}) + \frac{1}{6}u^3(\nu_h + \nu_{gh})^2 + \ldots \right). \end{aligned} \tag{A.8}$$

Comparing the two cumulant-generating functions (Eqs. A.6 and A.8), the first two terms of the two series are the same. That is to say, we can approximate $K_{\Delta\tau_g}(u) = K_{\Delta\tau}(u)$ with an error term that is third-order error in the variable u and second order in the episodicities ν_g and $\nu_g h$. The composite gamma process can therefore be closely approximated by a single gamma process with increments $\Delta\tau_g \sim \Gamma(\Delta t/(\nu_h + \nu_{gh}), \nu_h + \nu_{gh})$, and aggregate episodicity

$$\nu_g = \nu_{gh} + \nu_h, \tag{A.9}$$

which is simply the sum of the two contributing episodicities. To the best of our knowledge, this remarkable property characterizing the composition of two gamma processes had not been established before.

Appendix B. Moments of the gamma-subordinated OU process

In this appendix, we derive the time-evolving mean and variance of an Ornstein–Uhlenbeck process $Z(\tau)$ subordinated to a single gamma process $\tau(t)$. This is governed by the stochastic differential equation (SDE)

$$dZ = \lambda(z_\infty - Z)\,d\tau + \sigma\,dW(\tau), \tag{B.1}$$

where $\tau(t)$ has gamma-distributed increments $\Delta\tau \sim \Gamma(\Delta t/\nu, \nu)$. Here to make notations more compact we have set $\lambda = \lambda_g, \sigma = \sigma_g$ and $\nu = \nu_g$. Using variation of parameters, we can then derive explicit formulas for the time-evolving mean and variance of this approximate process. To start the derivation, we first define a function $g = g(Z, \tau) = Ze^{\lambda\tau}$. By the chain rule, the corresponding differential can be written

$$dg(Z, \tau) = d(Ze^{\lambda\tau}) = \lambda Ze^{\lambda\tau}\,d\tau + e^{\lambda\tau}\,dZ. \tag{B.2}$$

Substitution of Eq. (B.1) then yields

$$d(Ze^{\lambda\tau}) = e^{\lambda\tau}\lambda z_\infty\,d\tau + e^{\lambda\tau}\sigma\,dW(\tau). \tag{B.3}$$

We can then replace τ by a variable of integration u and integrate Eq. (B.3) from time 0 to t (Z from z_0 to $Z(t)$, u from 0 to $\tau(t)$) to get

$$Z(t)e^{\lambda\tau(t)} - z_0 = z_\infty(e^{\lambda\tau(t)} - 1) + \sigma\int_0^{\tau(t)} e^{\lambda u}\,dW(u). \tag{B.4}$$

Moving z_0 to the right hand side and dividing each side by $e^{\lambda\tau(t)}$, we obtain the solution

$$Z(t) = z_0 e^{-\lambda\tau(t)} + z_\infty(1 - e^{-\lambda\tau(t)}) + \sigma\int_0^{\tau(t)} e^{-\lambda(\tau(t)-u)}\,dW(u). \tag{B.5}$$

Taking the expectation, the third term averages out since $dW(u)$ is normally distributed. The expectation of the first two terms can be calculated as

$$\mathbb{E}[Z(t)] = \int_0^\infty (z_0 e^{-\lambda\tau} + z_\infty(1 - e^{-\lambda\tau}))f(\tau; t/\nu, \nu)\,d\tau. \tag{B.6}$$

where

$$f(\tau; t/\nu, \nu) = \frac{\nu^{-t/\nu}\tau^{t/\nu-1}e^{-\tau/\nu}}{\Gamma(t/\nu)} \tag{B.7}$$

is the probability density function (pdf) of the gamma-distributed τ. Therefore Eq. (B.6) can be rewritten into

$$\mathbb{E}[Z(t)] = \frac{(z_0 - z_\infty)\nu^{-t/\nu}}{\Gamma(t/\nu)}\int_0^\infty \tau^{t/\nu-1}e^{-\tau(\lambda+1/\nu)}\,d\tau + z_\infty\int_0^\infty f(\tau; t/\nu, \nu)\,d\tau, \tag{B.8}$$

where the integral of the gamma-distributed pdf from 0 to ∞ equals 1 and

$$\Gamma(t/\nu) = (\lambda + 1/\nu)^{t/\nu}\int_0^\infty \tau^{t/\nu-1}e^{-\tau(\lambda+1/\nu)}\,d\tau, \tag{B.9}$$

obtained by substituting $x = \tau(\lambda + 1/\nu)$ and $y = t/\nu$ into the definition of gamma function $\Gamma(y) = \int_0^\infty x^{y-1}e^{-x}\,dx$. We therefore obtain for the time-evolving mean the result

$$\begin{aligned}\mathbb{E}[Z(t)] &= (z_0 - z_\infty)(\lambda\nu + 1)^{-t/\nu} + z_\infty \\ &= z_0 + (z_\infty - z_0)\left(1 - (\lambda\nu + 1)^{-t/\nu}\right).\end{aligned} \tag{B.10}$$

The mean thus gradually transitions from the initial condition z_0 to the long term mean z_∞. Using the Itō isometry (Øksendal, 2000), the time-evolving variance can also be calculated as

$$\mathrm{Var}(Z(t)) = \mathbb{E}\left[\left(\sigma\int_0^\tau e^{-\lambda(\tau-u)}\,dW(u)\right)^2\right] = \mathbb{E}\left[\sigma^2\int_0^\tau e^{-2\lambda(\tau-u)}\,du\right]. \tag{B.11}$$

Integrating with the pdf of Eq. (B.7), we obtain for the time-evolving variance the result

$$\mathrm{Var}(Z(t)) = \sigma^2\int_0^\infty\int_0^\tau e^{-2\lambda(\tau-u)}\frac{\nu^{-t/\nu}\tau^{t/\nu-1}e^{-\tau/\nu}}{\Gamma(t/\nu)}\,du\,d\tau = \frac{\sigma^2}{2\lambda}\left(1 - (2\lambda\nu + 1)^{-t/\nu}\right), \tag{B.12}$$

which converges asymptotically towards a finite long term variance $\sigma_\infty^2 = \sigma^2/2\lambda$. To our knowledge, these results for the moments of a gamma-subordinated OU process had not been obtained before.

References

Anarde, K.A., Kameshwar, S., Irza, J.N., Nittrouer, J.A., Lorenzo-Trueba, J., Padgett, J.E., Sebastian, A., Bedient, P.B., 2018. Impacts of hurricane storm surge on infrastructure vulnerability for an evolving coastal landscape. Nat. Hazards Rev. 19, 04017020.

Baker, V.R., 1977. Stream-channel response to floods, with examples from central Texas. GSA Bull. 88, 1057–1071.

Barndorff-Nielsen, O.E., Shepard, N., 2001. Non-gaussian Ornstein-Uhlenbeck-based models and some of their uses in financial economics. J. R. Stat. Soc. Ser. B: Stat. Methodol. 63, 167–241.

Benda, L., Dunne, T., 1997. Stochastic forcing of sediment supply to channel networks from landsliding and debris flow. Water Resour. Res. 33, 2849–2863.

Brigo, D., Dalessandro, A., Neugebauer, M., Triki, F., 2009. A stochastic processes toolkit for risk management: Geometric Brownian motion, jumps, GARCH and variance gamma models. J. Risk Manag. Financ. Inst. 2, 365–393.

Brooks, G., Lawrence, D., 1999. The drainage of the Lake Ha! Ha! Reservoir and downstream geomorphic impacts along Ha! Ha! River, Saguenay Area, Quebec, Canada. Geomorphology 28, 141–168.

Bull, W.B., 1988. Floods; degradation and aggradation. John Wiley and Sons, New York.

Capart, H., Hsu, J.P.C., Lai, S.Y.J., Hsieh, M.L., 2010. Formation and decay of a tributary-dammed lake, Laonong River, Taiwan. Water Resour. Res. 46, 1–23.

Capart, H., Spinewine, B., Young, D.L., Zech, Y., Brooks, G., Leclerc, M., Secretan, Y., 1997. The 1996 Lake Ha! Ha! breakout flood, Québec: test data for geomorphic flood routing methods. J. Hydraul. Res. 45, 97–109.

Cenderelli, D.A., Wohl, E.E., 2003. Flow hydraulics and geomorphic effects of glacial-lake outburst floods in the Mount Everest region, Nepal. Earth Surf. Process. Landf. 28, 385–407.

Chien, F.C., Kuo, H.C., 2011. On the extreme rainfall of Typhoon Morakot (2009). J. Geophys. Res. Atmos. 116, D05104.

Davidson, S.L., Eaton, B.C., 2018. Beyond regime: A stochastic model of floods, bank erosion, and channel migration. Water Resour. Res. 54, 6282–6298.

Eagleson, P.S., 1978. Climate, soil, and vegetation: 2. The distribution of annual precipitation derived from observed storm sequences. Water Resour. Res. 14, 713–721.

Garcin, M., Poisson, B., Pouget, R., 2005. High rates of geomorphological processes in a tropical area: the Remparts River case study (Réunion Island, Indian Ocean). Geomorphology 67, 335–350.

Gardiner, C.W., et al., 1985. Handbook of stochastic methods, vol. 3. Springer, Berlin.

Gillespie, D.T., 1996. Exact numerical simulation of the Ornstein-Uhlenbeck process and its integral. Phys. Rev. E 54, 2084–2091.

Habtemicael, S., SenGupta, I., 2014. Ornstein-Uhlenbeck processes for geophysical data analysis. Phys. A 399, 147–156.

Hackl, J., Adey, B.T., Woźniak, M., Schümperlin, O., 2018. Use of unmanned aerial vehicle photogrammetry to obtain topographical information to improve bridge risk assessment. J. Infrastruct. Syst. 24, 04017041.

Hald, A., 1949. Maximum likelihood estimation of the parameters of a normal distribution which is truncated at a known point. Scand. Actuar. J. 1949, 119–134.

Hall, J.W., Meadowcroft, I.C., Lee, E.M., van Gelder, P.H., 2002. Stochastic simulation of episodic soft coastal cliff recession. Coast. Eng. 46, 159–174.

Hsieh, M.L., Capart, H., 2013. Late Holocene episodic river aggradation along the Lao-nong River (southwestern Taiwan): an application to the Tseng-wen Reservoir Transbasin Diversion Project. Eng. Geol. 159, 83–97.

Hsieh, M.L., Chyi, S.J., 2010. Late Quaternary mass-wasting records and formation of fan terraces in the Chen-yeo-lan and Lao-nung catchments, central-southern Taiwan. Quatern. Sci. Rev. 29, 1399–1418.

Johnson, P.A., Dock, D.A., 1998. Probabilistic bridge scour estimates. J. Hydraul. Eng. 124, 750–754.

Knox, J.C., 1996. Late Quaternary Upper Mississippi River alluvial episodes and their significance to the Lower Mississippi River system. Eng. Geol. 45, 263–285.

Kochel, R.C., 1988. Geomorphic impact of large floods: Review and new perspectives on magnitude and frequency. John Wiley and Sons, New York.

Korup, O., 2004. Landslide-induced river channel avulsions in mountain catchments of southwest New Zealand. Geomorphology 63, 57–80.

Lamb, R., Garside, P., Pant, R., Hall, J.W., 2019. A probabilistic model of the economic risk to Britain's railway network from bridge scour during floods. Risk Anal. 39, 2457–2478.

Lane, E.W., 1955. The importance of fluvial morphology in hydraulic engineering. Proc. Am. Soc. Civ. Eng. 81, 1–17.

Lapointe, M.F., Secretan, Y., Driscoll, S.N., Bergeron, N., Leclerc, M., 1998. Response of the Ha! Ha! River to the flood of July 1996 in the Saguenay region of Quebec: Large-scale avulsion in a glaciated valley. Water Resour. Res. 34, 2383–2392.

Lei, Y., Gu, H., Cui, P., 2022. Vulnerability assessment for buildings exposed to torrential hazards at Sichuan-Tibet transportation corridor. Eng. Geol. 308, 106803.

Lin, C., 2012. Bridge Hydraulics in View of Natural Disaster. Science and Technology Books Corporation (in Chinese).

Lin, C.H., Lin, M.L., 2015. Evolution of the large landslide induced by Typhoon Morakot: a case study in the Butangbunasi River, southern Taiwan using the discrete element method. Eng. Geol. 197, 172–187.

Lo, P.C., Lo, W., Chiu, Y.C., Wang, T.T., 2021. Movement characteristics of a creeping slope influenced by river erosion and aggradation: Study of Xinwulü River in southeastern Taiwan. Eng. Geol. 295, 106443.

Madan, D.B., Carr, P.P., Chang, E.C., 1998. The Variance Gamma process and option pricing. Eur. Finance Rev. 2, 79–105.

Madan, D.B., Seneta, E., 1990. The Variance Gamma (V.G.) model for share market returns. J. Bus. 63, 511–524.

Martinez-Villalobos, C., Neelin, J.D., 2019. Why do precipitation intensities tend to follow gamma distributions? J. Atmos. Sci. 76, 3611–3631.

Nolan, K.M., Marron, D.C., 1985. Contrast in stream-channel response to major storms in two mountainous areas of California. Geology 13, 135–138.

Øksendal, B., 2000. Stochastic Differential Equations. An Introduction with Applications. Springer, Berlin.

Pfeiffer, A.M., Collins, B.D., Anderson, S.W., Montgomery, D.R., Istanbulluoglu, E., 2019. River bed elevation variability reflects sediment supply, rather than peak flows, in the uplands of Washington State. Water Resour. Res. 55, 6795–6810.

Reitan, T., Petersen-Øverleir, A., 2011. Dynamic rating curve assessment in unstable rivers using Ornstein-Uhlenbeck processes. Water Resour. Res. 47, 1–14.

Ruiz-Villanueva, V., Badoux, A., Rickenmann, D., Böckli, M., Schläfli, S., Steeb, N., Stoffel, M., Rickli, C., 2018. Impacts of a large flood along a mountain river basin: the importance of channel widening and estimating the large wood budget in the upper Emme River (Switzerland). Earth Surf. Dyn. 6, 1115–1137.

Schumer, R., Jerolmack, D., McElroy, B., 2011. The stratigraphic filter and bias in measurement of geologic rates. Geophys. Res. Lett. 38, L11405.

Seier, G., Schöttl, S., Kellerer-Pirklbauer, A., Glück, R., Lieb, G.K., Hofstadler, D.N., Sulzer, W., 2020. Riverine sediment changes and channel pattern of a gravel-bed mountain torrent. Remote Sens. 12, 3065.

Stirzaker, D., 1999. Probability and random variables: a beginner's guide. Cambridge University Press.

Turowski, J.M., Badoux, A., Leuzinger, J., Hegglin, R., 2013. Large floods, alluvial overprint, and bedrock erosion. Earth Surf. Proc. Land. 38, 947–958.

Uhlenbeck, G.E., Ornstein, L.S., 1930. On the theory of the Brownian Motion. Phys. Rev. 36, 823–841.

Xiong, J., Tang, C., Tang, H., Chen, M., Zhang, X., Shi, Q., Chang, M., Gong, L., Li, N., Li, M., 2022. Long-term hillslope erosion and landslide–channel coupling in the area of the catastrophic Wenchuan earthquake. Eng. Geol. 305, 106727.

Yang, C.M., Chao, W.A., Weng, M.C., Fu, Y.Y., Chang, J.M., Huang, W.K., 2022. Outburst debris flow of Yusui stream caused by a large-scale Silabaku landslide, Southern Taiwan. Landslides 19, 1807–1811.

Yeh, C.H., 2012. Notes regarding the failure of 62 bridges due to Typhoon Morakot. Taiwan Highway Eng. 38, 2–19 (in Chinese).

Yochum, S.E., Sholtes, J.S., Scott, J.A., Bledsoe, B.P., 2017. Stream power framework for predicting geomorphic change: the 2013 Colorado front range flood. Geomorphology 292, 178–192.